Chapter 6

Interpretation Schemes

6.1 Introduction

In this chapter, we consider several possible interpretation schemes capable of reproducing the kinematic, spectral and luminosity behavior discussed in Chapters 3 and 5. A brief introduction will be given for the relevant aspects of several physical models of parsec–scale jets dealing with their spectral and kinematic properties. A model of compact relativistic jets (Blandford and Königl 1979; Königl 1981) will be used for studying the properties of the VLBI core, the closest region to the source of activity in 3C 345. A brief discussion will be presented on the models employing oblique shocks and plasma instabilities for explaining the observed properties of relativistic jets. We will adopt the shock–in–jet scenario (Marscher & Gear 1985), in order to relate the observed spectral and kinematic properties of the parsec–scale jet in 3C 345. We will attempt to verify the feasibility of the shock–in–jet scenario for explaining the observed kinematic and spectral evolution of C4 and C5.

6.1.1 Relativistic beaming

Relativistic beaming was suggested by Shklovsky (1963), to explain the observed asymmetric structure of M87 and 3C273. It was later combined with relativistic injection from galactic nuclei (Rees 1966, 1967). Accretion of matter on a central black hole (see Zeldovich 1964, Lynden-Bell 64, Salpeter 1964) is usually viewed as the most plausible mechanism causing this injection and originating relativistic jets in galaxies(Begelman *et al.* 1984). A *radiation–supported torus* (Piran 1982) or *ion–supported torus* (Rees 1985) were used to explain the formation of bipolar ultra relativistic outflows in AGN. A jet can consist either of a relativistic $e^{\pm}$ plasma, or a combination of a thermal $e^{\pm} - p$ (*underlying jet*) and relativistic $e^{-} - e^{+}$ (*beam*) plasma, with possible relativistic $e^{\pm}$ injection from the vicinity of the black hole (cf. Camenzind 1993) The former possibility has been giving rise to various shock models (cf. Marscher 1990, Hughes, Aller & Aller 1991, Valtaoja 1992), and the latter possibility has led to a suggestion of the *two–fluid* model (Pelletier & Roland

1989).

Presence of shocked regions in the jet is usually deduced from the polarization observations revealing high linear polarization in bright components emission (see Brown *et al.* 1994). The two–fluid scenario can be supported by the detection of two different velocities in the jet of NGC 1275 (Marr *et al.* 1989), and observation of limb brightening in the jet of M87 (Reid *et al.* 1989).

6.1.2 Jet formation and acceleration

The jets are believed to be formed in the vicinity of an accretion disk around a supermassive black hole in the center of AGN. The rotation of the disk can produce the toroidally shaped magnetic field collimating the outflowing material into two bipolar streams that can be accelerated up to ultra-relativistic speeds (see reviews by Begelman, Blandford, & Rees, 1984; Begelman 1995). The source of acceleration of an $e^{\pm}$ plasma to relativistic velocities has been sought in various physical processes involving interactions with radiation (e.g. Trussoni *et al.* 1992; Henri and Pelletier 1991), and with the thermal plasma component of the jet. Marscher (1980) considered adiabatic acceleration; Reynolds (1982) studied MHD accelerating jets; Conçalves *et al.* (1993) suggested a model with turbulent acceleration; Kirk and Schneider (1987) investigated acceleration by Fermi processes. Several models predict the generation of the radiating particles to occur farther down the jet, owing to $e^{\pm}$ cascade processes (Mannheim 1993; Blandford & Levinson 1995), or to the decay of ultrarelativistic neutrons (Eichler & Wiita 1978; Giovanoni & Kazanas 1990) that may result in formation of a standing shock observed as the VLBI core (Marscher & Daly 1988).

The observed extended lifetime of superluminal components may require an additional reacceleration or another factor maintaining the component emissivity along the jet. (C4, for instance, has been observed for 14 years now, which translates into more than 110 years in the reference frame of a jet moving with $\gamma \approx 10$, $\theta \approx 5°$.) Königl (1981) included reacceleration of electrons in shocks, to compensate energy losses. Interactions between relativistic and thermal components of the jet can be essential in the two–fluid scenario (Sol *et al.* 1989), regardless to whether a relativistic beam permeates the jet (Pelletier & Sol 1992), or propagates in a channel through the jet (Pelletier & Roland 1990). Rose *et al.* (1984, 1987) showed that such interactions can lead to heating and acceleration of the thermal plasma, and to $e^{\pm}$ pair production. In case of precession driven helical geometry of the jet, intensity of the interactions will also depend on kinematic characteristics of the jet (Roland *et al.* 1994). We have suggested elsewhere (Lobanov and Zensus 1994) that such a scheme may be capable of explaining the observed spectral evolution of the jet in 3C345.

6.2 Selected aspects of relativistic shock models

In this section we describe the main features of a generic relativistic shock model, and give a qualitative description of two specific topics of the jet models: a) the frequency

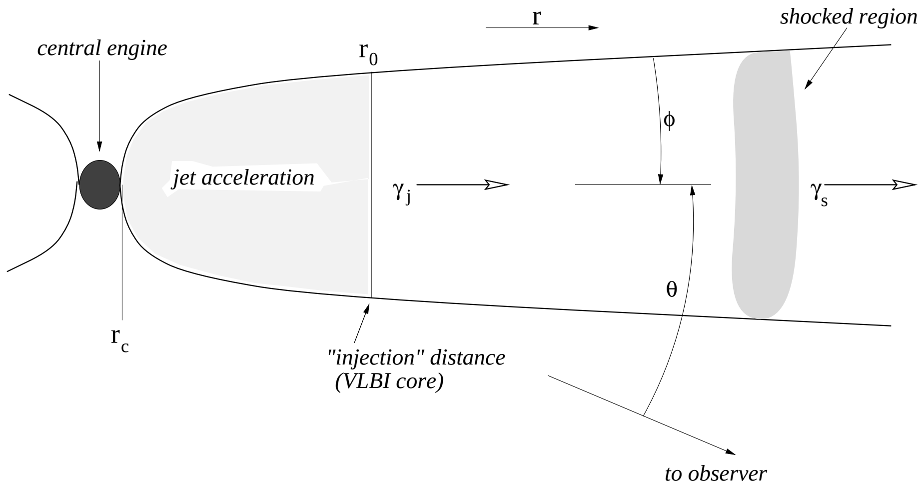

Figure 6.1: Basic outlines of the relativistic jet model.

dependent shift of the core poisition; and b) the spectral evolution of a relativistic shock. These description will be subsequently used for an interpretation of the VLBI observation described in the previous chapters.

6.2.1 Relativistic shock models

Relativistic shocks propagating down a conical jet were first suggested by Blandford and Rees (1978) to explain the knots moving at apparent superluminal speeds as observed in VLBI images. Subsequently, the model has been developed in a number of works (i.e. Blandford and Königl 1979; Marscher 1980; Königl 1981; Reynolds 1982; Ghisellini, Maraschi and Treves 1985). A sketch of main features of the generic relativistic jet model is given in Figure 6.1.

A region of significant particle acceleration is assumed to exist at the extreme center of an AGN. The jet can contain both protons, and electron-positron pairs. The accelerated particles are confined by the surrounding plasma, with steep pressure and density gradients along the rotational axis of the central engine. Interactions between the jet and the ambient medium are usually ignored, and the jet itself is assumed to have no transverse velocity gradient. A "nozzle" is formed at the distance r_c where the flow becomes supersonic ($\gamma_c = 1.22$). Approaching the nozzle, the initially disordered magnetic field becomes amplified (due to particle compression) and stretched along the direction of flow. Beyond the nozzle, the flow is accelerated by the conversion of internal relativistic particle energy γ_e to bulk kinetic energy γ_j, so that $\gamma_j \propto \gamma_e \propto r^\epsilon$ (ϵ =const). The resulting particle energy distribution $N(\gamma_e)$ can be approximated by the power law:

$$N(\gamma_e) = N_0 \gamma_e^{-s} \text{ for } \gamma_1(r) < \gamma_e < \gamma_2(r)\,, \tag{6.1}$$

where s is the particle energy spectral index. The jet is assumed to have constant Lorentz factor γ_j, and form an angle θ with the line of sight. The jet geometry can be approximated by a conical or paraboloidal expansion, with the transverse radius

$$R = a\, r^{\varepsilon}, \quad \text{with } \varepsilon \leq 1, \;\; r_c \leq r \leq r_{max}, \tag{6.2}$$

where r_{max} can be taken $\sim 100\, r_0$, for most of parsec-scale jets. The jet opening angle $\phi = \arctan(R/r)$ is constant for $\varepsilon = 1$. In what follows, we will consider only constant opening angle jets. The magnetic field and particle density decrease with r, and can be approximated as:

$$B = B_1 (r_0/r)^{-m} \tag{6.3}$$

$$N = N_1 (r_0/r)^{-n}\,, \tag{6.4}$$

where B_1, N_1 are the magnetic field and the electron density at $r_0 = 1\,\mathrm{pc}$. Königl (1981) shows that the combination $m = 1$, $n = 2$, can describe the observed X-ray and synchrotron emission from the most compact regions of the jet.

6.2.2 VLBI core and ultracompact jet

In the scheme in Figure 6.1, outside the radius r_0 the protons become subrelativistic in the rest frame of the flow, and the bulk Lorentz factor freezes at the value $\sim \gamma_j = \gamma(r_0)$. This location in the jet is most likely to be observed as the VLBI core (Marscher 1995). It is also referred to as the "injection point" (at which the relativstic plasma is asssumed to be injected into the jet at γ_j), in most of the models dealing with parsec-scale relativistic jets. Theoretically, the VLBI core lies in the narrow end of an undisturbed jet flow. Anywhere outside the nozzle distance r_c, the properties of the undisturbed jet emission are similar to those of an inhomogeneous synchrotron source—a condition that is used for describing the emission of the VLBI core.

A general description of synchrotron emission can be given by the volume emissivity, j^s_ν, and absorption coefficient κ^s_ν (Ginzburg and Syrovatskii 1964; Blumenthal and Gould 1970):

$$j^s_\nu = C_1(\alpha_0) K_0 B^{1-\alpha_0} \nu^{\alpha_0} (r_0/r)^{[n+m(1-\alpha_0)]}\,, \tag{6.5}$$

$$\kappa^s_\nu = D_1(\alpha_0) K_0 B_0^{1.5-\alpha_0} \nu^{\alpha_0 - 2.5} (r_0/r)^{[n+m(1.5-\alpha_0)]}\,, \tag{6.6}$$

where $\alpha = (1-s)/2$ is the spectral index defined as $S_v \propto \nu^{\alpha}$. The functions $C_1(\alpha)$, and $D_1(\alpha)$ are tabulated in Blumenthal and Gould (1970). The first order approximations of these functions are:

$$\ln C_1(\alpha) \approx -49.76793 - 14.70086\alpha\ , \tag{6.7}$$

$$\ln D_1(\alpha) \approx 17.40964 - 15.72085\alpha \tag{6.8}$$

Because of the synchrotron self-absorption, the jet spectrum will have a maximum at frequency ν_m (the peak frequency) at which the optical depth of the jet is τ_m. It can be shown (e.g. Pacholczyk 1970) that

$$e^{\tau_{max}} = 1 + \tau_{max}(1 - 0.4\alpha) \tag{6.9}$$

Then, the peak flux density S_m of the synchrotron emission, and the corresponding optical depth τ_m are (Marscher 1987):

$$S_m = \frac{\pi}{6} C_S(\alpha) N_0 B^{1-\alpha} \nu_m^{\alpha} d_\Omega^3 D_L (1+z)^{\alpha-1} \delta_j^3 - \alpha \,, \tag{6.10}$$

$$\tau_m = C_\tau(\alpha) N_0 B^{1.5-\alpha} \nu_m^{-(2.5+\alpha)} d_\Omega D_L (1+z)^{\alpha-4.5} \delta_j^{2.5-\alpha} \,, \tag{6.11}$$

where D_L is the luminosity distance to the source; d_Ω is the source angular diameter measured in milliarcseconds. The functions $C_S(\alpha)$, $C_\tau(\alpha)$ are approximated by:

$$\ln C_S(\alpha) \approx -97.72775 - 362.76822\alpha - 642.31450\alpha^2 - 367.60167\alpha^3 \tag{6.12}$$

$$\ln C_\tau(\alpha) \approx 17.55006 - 43.55758\alpha \tag{6.13}$$

If the turnover frequency and turnover flux density are known from observations, then the magnetic field B, and electron density N_0 can be calculated from Equations (6.10)-(6.11):

$$B = 10^{-5} C_B(\alpha) d_\Omega^4 \nu_m^5 S_m^{-2} \delta_j (1+z)^{-1} \quad [\mathrm{G}] \tag{6.14}$$

$$N_0 = C_N(\alpha) D_L^{-1} d_\Omega^{4\alpha-7} \nu_m^{4\alpha-5} S_m^{3-2\alpha} (1+z)^{6-2\alpha} \delta_j^{2\alpha-4} \,, \tag{6.15}$$

where D_L is in Gpc, and ν_m is in GHz. The functions $C_B(\alpha)$, and $C_N(\alpha)$ are given by:

$$C_B(\alpha) \approx -1.4 - 17.66667\alpha - 20.8\alpha^2 - 8.53333\alpha^3 \tag{6.16}$$

$$\ln C_N(\alpha) \approx 5.58446 + 14.46639\alpha + 1.45463\alpha^2 \tag{6.17}$$

The magnetic field in the ultracompact jet can also be derived from the frequency dependent shift of the VLBI core position measured in Chapter 4.

6.2.3 Physics of the core shift

At any given frequency the VLBI core is observed at the location at which the optical depth of synchrotron self-absoprtion is $\tau_s = 1$ (see the sketch in Figure 4.5). The frequency ν_s at which it occurs can be found from Equation (6.11) (Königl 1981):

$$\nu_s(r) \approx F_s(N_1, \delta_j, z, \phi, \theta) B_1^{k_b} r^{-k_r} \ \mathrm{Hz}, \tag{6.18}$$

where B_1 is the magnetic field at $r = 1\,\mathrm{pc}$, and k_r, k_b, and F_s are given by the following formulae:

$$k_r = \frac{(3-2\alpha)m + 2n - 2}{5-2\alpha}. \tag{6.19}$$

$$k_b = \frac{3-2\alpha}{5-2\alpha} \tag{6.20}$$

$$F_s(N_1, \delta_j, z, \phi, \theta) = (1+z)^{-1} [6.2 \times 10^{18} C_2(\alpha) \delta_j^{1.5-\alpha} N_1 \phi \csc\theta]^{1/2.5-\alpha}, \tag{6.21}$$

where $C_2(\alpha) = 8.4 \times 10^{10}$, for $\alpha = -0.5$ (Blumenthal and Gould 1970). All quantities are in *cgs* units, except r which is expressed in parsecs. From Equation (6.18), the distance at which the spectral index is flat at frequency ν_s is

$$r_{pc} = F_s^{1/k_r} \nu_s^{-1/k_r} B_1^{k_b/k_r} \tag{6.22}$$

Therefore, if the core positions measured at two frequencies ν_1, ν_2 are different by Δr_{mas} the corresponding magnetic field is

$$B_1 \approx \left[\frac{\Delta r_{mas} D_L}{(1+z)^2 \sin\theta} \cdot \frac{\nu_1^{1/k_r} \nu_2^{1/k_r}}{\nu_2^{1/k_r} - \nu_1^{1/k_r}} \right]^{k_r/k_b} F_s^{-\frac{1}{k_b}}, \tag{6.23}$$

where D_L is the luminosity distance to the source. For 3C 345, we obtain $B_1 = 2.4 \pm 0.4$ G, for a jet with $\gamma_j = 10$, $\theta_j = 5°$, $\phi = 1°$. The particle number density $N_1 \approx 10^2\,\mathrm{cm}^{-2}$, from the synchrotron self-Compton models applied to 3C 345 (ZCU95, Ghisellini *et al.* 1992). If B_1 is known, then Equation (6.22) can be used for calculating the distance of VLBI core from the true origin of the jet. Using the calculated distance, and applying the assumption $B = B_1 r^{-m}$ made earlier, we can write for the magnetic field in the VLBI core:

$$B_{core}(\nu) \approx \nu^{m/k_r} \left[\frac{\Delta r_{mas} D_L}{(1+z)^2 \sin\theta} \cdot \frac{\nu_1^{1/k_r} \nu_2^{1/k_r}}{\nu_2^{1/k_r} - \nu_1^{1/k_r}} \right]^{\frac{k_r - m k_b}{k_r}} F_s^{-\frac{1}{k_b}} \tag{6.24}$$

For a jet corresponding to the dependence in Figure 4.6, we can have $m = 1$, $n = 2$, $\alpha = -0.5$. In this case, Equation (6.24) becomes

$$B_{core}(\nu) \approx 3.05 \times 10^{-3} \cdot \frac{\nu}{\delta_j} \left[\frac{\Delta r_{mas} D_L (1+z)}{N_1 \phi} \cdot \frac{\nu_1 \nu_2}{\nu_2 - \nu_1} \right]^{1/2} [\mathrm{G}], \tag{6.25}$$

with D_L measured in Mpc, and all frequencies given in GHz. As seen from this equation, the estimate is sensitive to the jet Doppler factor. Therefore, to obtain a reliable estimates of magnetic field, the jet geometry must be well known. To derive a plausible value of δ_j, we can assume that the jet follows the path of least kinetic power such that the jet Lorentz factor $\gamma_j = (1 + \beta_{app}^2)^{0.5}$ along the entire jet (this assumption is valid only if the observed speeds are those of bulk motion in the jet, but not the pattern speeds). Under this condition, the variations of viewing angle can be derived for the jet components in the immediate vicinity of the core, and the viewing angle of the ultracompact jet can be estimated. In 3C 345, this gives $\theta_j \approx 5°$.

6.2.4 Spectral evolution in the plane shock model

In the scheme shown in Figure 6.1, relativistic shocks propagating at the pattern speed γ_p can be formed at $r > r_0$, resulting in significant amplification of synchrotron emission due to magnetic field compression in the shocked regions. It is possible to describe the basic evolution of a synchrotron emitting relativistic shock by following the changes of its turnover flux and turnover frequency, S_m and ν_m. Marscher and Gear (1985) proposed the "shock-in-jet" scenario in which the radiation is originated from a plane shock embedded in the jet. In this scheme,

$$S(\nu) \propto B^{(s+1)/2} \nu^{-(s-1)/2} r^2 \Delta x \ , \tag{6.26}$$

where $\Delta x \ll R$ is the depth of shocked region. The shock is expanding sideways adiabatically, and maintains the condition of a plane shock, so that its longitudinal dimension is much smaller than the transverse. The magnetic field is assumed to fall off as r^{-m} with $m = 1$ for a field perpendicular to the jet axis, and $m = 2$ for the field parallel to the axis (note that there can also be intermediate values of m). We follow Marscher 1990, and consider the same three stages of the shock evolution: Compton loss, synchrotron loss, and adiabatic loss stage. For each of these stages, the spectrum of the shock emission as received in the observer's frame can be written in the form

$$S(\nu) \propto r^{\xi} \nu^{-\zeta} \delta^{(s+3)/2} \tag{6.27}$$

where s is electron energy distribution spectral index; ξ and ζ are stage dependent indices.
The turnover flux and frequency are defined in the shock-in-jet model as the spectral point corresponding to optical depth $\tau = 1$ (cf. Cawthorne 1991)

$$S(\nu_m) \propto B^{-1/2} \nu_m^{5/2} r^2 \propto r^{(4+m)/2} \nu_m^{5/2} \tag{6.28}$$

Following the scheme of Marscher, we further assume Doppler factor $\delta \propto r^b$, where b is a constant. In general, b can vary with radius r and, correspondingly, with time t. For simplicity, we ignore these variations.

Combining (6.27) and(6.28), we obtain for the turnover frequency

$$\nu_m \propto r^{[\xi-(4+m)/2+b(s+3)/2]/[5/2+\zeta]} \tag{6.29}$$

Using ξ and ζ derived by Marscher (1990), we write expressions for ν_m at each stage of the shock development.

1. *Compton–loss stage* $(\xi = [(11-s) - m(s+1)]/8; \quad \zeta = -s/2)$

$$\nu_m \propto r^{-[(5+s)(m+1)-4b(s+3)]/[4(s+5)]} \tag{6.30}$$

2. *Synchrotron–loss stage* $(\xi = -[4(s-1) + 3m(s+1)]/6; \quad \zeta = -(s-1)/2)$

$$\nu_m \propto r^{-[3m(s-1)+4(s+2)-3b(s+3)]/[3(s+5)]} \tag{6.31}$$

3. *Adiabatic–loss stage* $(\xi = [2(5-2s) - 3m(s+1)]/6; \quad \zeta = -(s-1)/2)$

$$\nu_m \propto r^{-[2(2s+1)+3m(s+2)-3b(s+3)]/[3(s+4)]} \tag{6.32}$$

r in formulae (6.30)–(6.32) is still measured in the rest frame of the jet, and it should be transformed into quantities measured in the observer's frame, taking into account the time dependence of Doppler factor. Assuming that the shock propagates down the jet with the instant velocity $\beta(t)$ forming the angle $\theta(t)$ with the line of sight, we can derive

$$r = (1+z)^{-1} \int \frac{\beta(t)}{1-\beta(t)\cos\theta(t)} dt \qquad (6.33)$$

We will be using this description for interpretation of the observed turnover frequency evolution of the superluminal features, C4 and C5, in the jet of 3C 345.

6.2.5 Oblique shocks and plasma instabilities

Increasing complexity of the observed properties of the jets has led to more sophisticated jet models that incorporate possible transverse velocity gradients in the jet, and interactions between physically different plasma components of the jet. Several studies of magnetized jet formations suggest that parsec-scale jets can be formed with a fast ($\gamma_e \approx 10-100$) ultrarelativistic beam (Begelman 1995; Ustyugova *et al.* 1995) surrounded by a slower, mildly relativistic (Begelman 1995), or non-relativistic (Sol *et al.* 1989) outflow. In such jets, oblique shocks and plasma instabilities are likely to be produced due to the interaction between the beam and the outflow. It has been shown that such a situation can succesfully explain several observed properties of large-scale jets (Laing 1993, 1995; Bicknell & Begelman 1996)

A number of studies have shown that a relativistic plasma beam moving through an external medium is unstable against Kelvin–Helmholtz perturbations. The beam expands adiabatically while remaining in pressure balance with the ambient medium that may be represented by the interstellar matter (Hardee 1982) or a thermal outflow from the accretion disk (Sol *et al.* 1989). A discontinuity is expected to form at the limiting surface between the two compressible relativistic fluids (Blandford & Pringle 1976). In case of cylindrical symmetry of the beam, the adiabatic perturbations of relativistic fluid, with Lorentz factor γ and adiabatic exponent Γ, are given by (e.g. Ferrari *et al.* 1978):

$$\gamma^2 \left(\rho + \frac{P}{c^2}\right) \frac{d\mathbf{v}}{dt} = -\left[\nabla P + \frac{\mathbf{v}\partial P}{c^2 \partial t}\right] \qquad (6.34)$$

$$\gamma \frac{d\rho}{dt} + \left(\rho + \frac{P}{c^2}\right)\left[\frac{\partial \gamma}{\partial t} + \nabla \cdot (\gamma \mathbf{v})\right] = 0\,, \qquad (6.35)$$

$$\frac{d}{dt}(P\rho^{-\Gamma}) = 0\,, \qquad (6.36)$$

where ρ is the proper density, P is the gas pressure. It is assumed that the sound speed $\beta_s \ll 1$, measured in the frame of the fluid. In cylindrical coordinates (r, ϕ, z), with z-axis coinciding with the beam axis, a linearized form of the perturbations can be represented by the Fourier expansion with harmonics of the form

$$\mathcal{F}(r,\phi,z) = \mathcal{G}(r) \exp i(kz + n\phi - \omega t). \qquad (6.37)$$

$\mathcal{G}(r)$ is the amplitude of perturbation; ω is the frequency, and k and n are the parallel and transverse wavenumbers of harmonic component. The pinching ($n = 0$), helical ($n = 1$) and elliptical ($n = 2$) modes are most likely to affect the jet boundary and kinematics, although the higher modes can also be present. The higher modes are expected to be most prominent at large scales (Hardee 1996), and we will neglect them in the following considerations.

The evolution of $\mathcal{G}$ can be determined from the relativistic dispersion relation (e.g. Hardee 1984, 1986; Hardee, Cooper and Clark 1994), so that $\mathcal{G}(r) \propto \exp[1-(r_0/r)^{0.5}]$. The maximum amplitude of a perturbation with frequency ω_0 is then given by

$$\mathcal{G}(r)_{max} \approx \mathcal{G}(r_0) \exp\left[\frac{2\omega_0 r_0}{\beta_j \gamma \eta_0^{0.5} \sin\psi}\right], \tag{6.38}$$

where ψ is the jet half–opening angle; r_0 is the jet size in the location of origin of the perturbation; $\eta_0 = \rho_{in}/\rho_{ex} \propto \rho^{(\gamma_{in}/\gamma_{ex}-1)}$ is the gas density ratio of the beam and the external plasma. Hardee (1984) shows that the frequency, ω_s of the fastest spatially growing perturbation can be considered independent from the jet density and Mach number; so that $\omega_s \approx 0.1(\frac{\beta_j}{r})$, resulting in the following form for $\mathcal{G}(r)$ (Hardee 1986)

$$\mathcal{G}(r) = \mathcal{G}(r_0) \exp\left\{\left[\frac{0.134\, r_0}{\gamma_j \eta_0^{0.5} \sin\psi}\right]\left[1 - \left(\frac{r_0}{r}\right)^{0.5}\right]\right\}, \tag{6.39}$$

For the fastest temporally growing mode Hardee (1984) gives

$$\mathcal{G}(r) \sim \mathcal{G}(r_0)(r/r_0)^{0.83/M_{in}\sin\psi}, \tag{6.40}$$

where M_{in} is the Mach number of the beam. This expression can be approximated, for the case of simple model of perturbed relativistic beam (Roland *et al.* 1994)

$$\mathcal{G}(r) \sim \frac{\mathcal{G}(r_0) r}{a_0 + r}, \tag{6.41}$$

with a_0 being a model dependent constant.

Three-dimensional hydrodynamical simulations of Kelvin-Helmholtz instabilities developing in the jet show (Hardee *et al.* 1995) show that the unstable surface modes and the elliptical mode appear to be coupled to the precessionally driven helical mode. The helical internal body mode is found to be responsible for the short length velocity oscillation along the jet axis. The resulting patterns of the velocity field and particle density (see Figures 3 and 6 in Hardee *et al.* 1995) resemble those of the gradients of the turnover frequency observed in the extended jet of 3C 345 (Chapter 4, Figure 4.22). As was argued in Chapter 4, the turnover frequency is exceptionally sensitive to velocity and density variations, and therefore the observed gradients of the turnover frequency may reflect the presense of an internal helical body mode of Kelvin-Helmholtz instability developing in the underlying jet of 3C 345. This question, however, should be addressed properly by using low frequency observations, and reliably determining the turnover frequency variations in the underlying jet.

6.2.6 Kinematic model for a perturbed jet

A more simplistic approach to the problem of interaction between relativistic and non-relativistic matter in the jet is employed by the two-fluid model (Sol *et al.* 1989). The jet is assumed to consist of an ultrarelativistic ($\gamma \approx 10$) $e^{\pm}$ beam surrounded by a thermal outflow with $\beta \approx 0.4 - 0.5$. The relativistic beam is perturbed, and can be precessing with the characteristic period P_0, and angle Ω_0. Roland *et al.* (1994) show that this model can explain the observed short-term variability of 3C 273, and also make plausible predictions about the kinematics of superluminal features in the parsec-scale jets. The trajectories of relativistic components are determined by collimation in the magnetic field of the perturbed beam (Roland *et al.* 1994), and can be approximated by a helical path. In the coordinate system (x,y,z) with z–axis coinciding with the rotational axis of the helix, the component's position is given by

$$\left\{ \begin{array}{lcl} x & = & r(z)\cos(\omega t \,-\, kz \,+\, \phi_0) \\ y & = & r(z)\sin(\omega t \,-\, kz \,+\, \phi_0) \\ z & = & z(t), \end{array} \right. \tag{6.42}$$

where $r(z)$ describes the amplitude of helix, and can be approximated by equation (6.41). For a precessing beam, we can write for a_0:

$$a_0 = r_0/\tan\Omega_0 \tag{6.43}$$

The form of function $z(t)$ should be determined from the evolution of the velocity $\vec{\beta}_b$ of relativistic component. From (6.42)

$$\left\{ \begin{array}{lcl} \beta_x & = & \beta_z r'_z(z)\cos(\omega t \,-\, kz \,+\, \phi_0) - r(z)\,(\omega - k\beta_z)\sin(\omega t \,-\, kz \,+\, \phi_0) \\ \beta_y & = & \beta_z r'_z(z)\sin(\omega t \,-\, kz \,+\, \phi_0) + r(z)\,(\omega - k\beta_z)\cos(\omega t \,-\, kz \,+\, \phi_0) \\ \beta_z & = & z'_t, \end{array} \right. \tag{6.44}$$

so that

$$\beta_b^2 = (z'_t)^2 C_1(z) + r^2(z)\,(\omega - kz'_t)^2\,, \tag{6.45}$$

where $C_1(z) = [r'_z(z)]^2 + 1$. With assumptions made about the beam velocity $\vec{\beta}_b$ and geometry $r(z)$, equation (6.45) can be solved for $z(t)$ numerically, and the beam trajectory can be determined. A plausible form for $r(z)$ can be obtained from equations (6.37)–(6.39). The beam velocity $\vec{\beta}_b$ can be conveniently expressed as a function of z, and in the simplest case viewed as constant. Then, under the condition of initial acceleration of the beam ($dz/dt > 0$, for $z \to 0_+$), equation (6.45) has a unique solution

$$t(z) = t_0 + \int_{z_0}^{z} \frac{C_2(z)}{k\omega r^2(z) + [C_2(z)\beta_b^2 - \omega^2 r^2(z) C_1(z)]^{1/2}} dz\ , \tag{6.46}$$

with $C_2(z) = C_1(z) + k^2 r^2(z)$. Generally, both ω and k can also vary. Their variations should be then represented with respect to z, in order to preserve the solution given

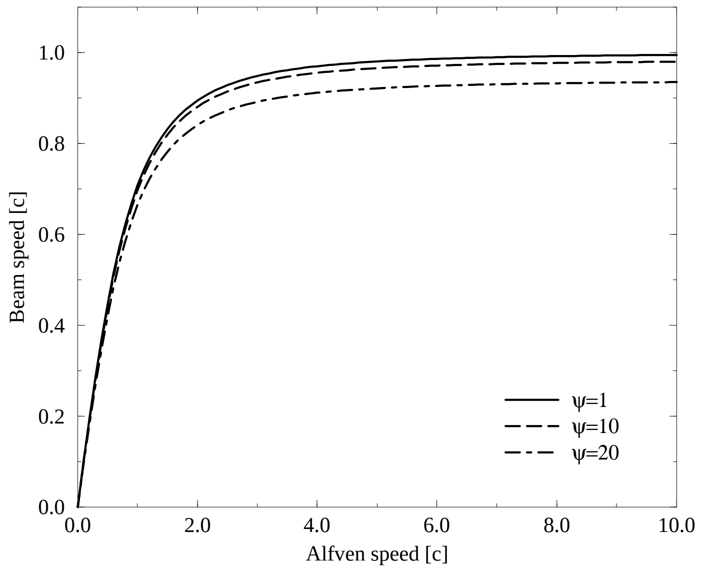

Figure 6.2: Changes of limiting beam speed as a function of Alfvèn speed in the beam plasma. The curves are shown for different local half–opening angles of the beam. In case of variable $\psi(z)$, the corresponding curve would oscillate between the shown limits.

by (6.46). Numerical methods should be used otherwise. The solution (6.46) can be found for all $r(z)$ not exceeding the limit of

$$r(z) \leq \beta_b \left[\omega^2 - k^2 \beta_b^2 \cos^2 \psi(z)\right]^{-0.5} \tag{6.47}$$

The beam half–opening angle $\psi(z) = \arctan(r'_z)$ in (6.47) is measured locally (as opposed to the "global" opening half–angle $\psi_g(z) = \arctan[r(z)/z]$), and describes the evolution of the amplitude of helix. For a jet with constant opening angle ($\psi(z) = \psi = const$), the inequality (6.47) can be rewritten as:

$$z \leq \beta_b \left[\omega^2 \tan^2 \psi - k^2 \beta_b^2 \sin^2 \psi\right]^{-0.5} \tag{6.48}$$

The beam velocity β_b and local half–opening angle ψ should satisfy the condition:

$$\beta_b \cos \psi \leq \frac{V_A}{\sqrt{V_A^2 + 1}}\,, \tag{6.49}$$

where $V_A = V_A/c$ is Alfvèn speed measured in units of the speed of light. The beam speed does not depend strongly on ψ (see Figure 6.2). The beam speed changes in Figure 6.2 follow roughly the ratio ω/k required by the kinematic model. Once we have determined the velocity components $\beta_{x,y,z}$, we can find the beam viewing angle

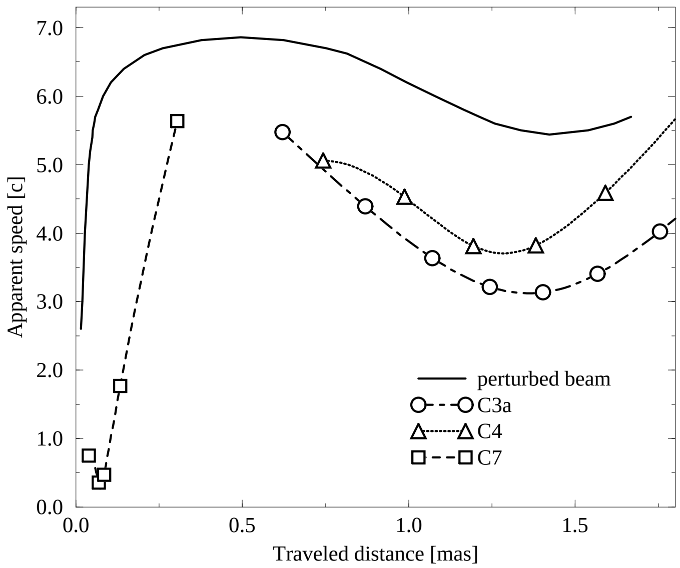

Figure 6.3: Perturbed beam model, and the measured apparent speeds of the strongest superluminal features in 3C 345. The model curve (Roland 1996, private communication) corresponds to a perturbed beam with the perturbation period $P_0 = 1500$ years. The perturbation can be caused by the orbital motion in a binary black hole system in the center of 3C 345.

θ_b, and calculate the apparent velocity $\beta_{app} = \beta_b \sin\theta_b(1 - \beta\cos\theta_b)^{-1}$. The model evolution of β_{app} can be compared with the observed β_{app} for the closest superluminal features. Figure 6.3 shows the apparent speed evolution for the perturbed beam model with $\gamma_j = 10$, $P_0 = 1500$ years, $\Omega_0 = 2^{\circ}$ (Roland 1996, private communication). For comparison, the derived apparent speeds are plotted for C3a, C4, and C7. The perturbed beam shows a characteristic decrease of its apparent speed similar to that seen in C3a, and C4. A steep rise of the model predicted apparent speed at early evolutionary stages also consistent with the observed speed changes in C7. These facts may suggest that the earliest stages of the component kinematic evolution may be produced by an instability developing in the jet. This can also provide evidence for a possible relationship between shocks and instabilities in the jet. Bicknell and Begelman (1996) have suggested that Kelvin-Helmholtz instabilities may actually produce shocks by deflecting the supersonic flow. Such shocks should be oblique, and should move at speeds lower than the jet flow speed. There's no conclusive answer about the speed of the underlying jet on parsec-scales, and therefore the possibility of plasma instabilities originating, and co-existing with the shocks down to very compact scales should be explored.

6.3 Interpretation of the VLBI osbservations of 3C 345

In this section, we will discuss the ultra-compact jet of 3C 345, and attempt to describe the observed spectral evolution of the jet in the framework of a rather simplistic shock model. The properties of ultracompact jet are derived from the core position offset (measured in Chapter 4) based on the theoretical model described in Section 6.2.3. The analysis of the spectral evolution is based on the turnover frequency evolution of C4 and C5 (see Chapter 4), and the shock-in-jet model described in Section 6.2.4.

6.3.1 Properties of ultracompact jet in 3C 345

In Section 6.2.3, we have determined the value of magnetic field $B_1 \approx 2.3 \pm 0.4\,\mathrm{G}$, at 1 pc away from the central engine of the AGN. Using the equations derived in that section, we can now calculate the magnetic field in the core at various frequencies, and both the linear and angular offsets of the core position from the true jet origin. We use Königl's (1979) model to calculate the brightness temperature in the core, and give an estimate of the total power and the synchrotron power of the ultracompact jet. The total (kinetic + magnetic field) power of the ultracompact jet is:

$$L_t \approx 0.75\,\Theta(3 + 2\,k_e\Lambda)\gamma_j^2\beta_j^2 c B^2 r^2 \phi^2 \ , \tag{6.50}$$

where $k_e \approx 1$, and $\Lambda = \ln(\gamma_{max}/\gamma_{min})$; $\Theta = \ln(r_{max}/r_{min})$ is the range of the jet extensions from which the emission is received. The average total power of the jet $L_t \approx (2.3 \pm 0.4) \times 10^{47}\,\mathrm{erg/s}$. The synchrotron luminosity:

$$L_{syn} \approx \frac{3k_e L_t}{6 + 4k_e\Lambda} \tag{6.51}$$

In 3C 345, we find $L_s \approx (2.9\pm0.5)\times10^{46}\,\mathrm{erg/s}$. The maximum brightness temperature is (Königl 1979):

$$T_{b\,max} \approx 6.5 \times 10^7 \frac{\delta_j^{5/6}}{(1+z)} \left[\frac{3k_e^2 L_t}{(3+2k_e\Lambda)\Theta\gamma_j^2\beta_j(\sin\theta)^4(\phi_{ob})^2}\right]^{1/12} , \tag{6.52}$$

where $\phi_{ob} = \phi/\sin\theta$ is the observed jet opening angle. With the derived magnetic field, the maximum brightness temperature is $T_{b\,max} \approx (4.26 \pm 0.06) \times 10^{12}\,\mathrm{K}$. The obtained value is consistent with the $10^{12}\,\mathrm{K}$ inverse Compton limit, similarly to the mean values of the maximum brightness temperature in a sample of superluminal sources (Vermeulen & Cohen 1994). Arguments based on the hypothesis of equipartition between relativistic particle and magnetic energy density ($\varepsilon_p/\varepsilon_B \sim 1$) predict a lower value of the maximium brightness temperature ($T_{b\,eq} \approx 4.5 \times 10^{11}\,\mathrm{K}$, Readhead 1994). The ratio $T_{b\,max}/T_{b\,eq}$ can indicate how different are the physical conditions

Table 6.1: Derived parameters of the ultracompact jet

ν [GHz]	B_{core} [G]	Δr_{pc}	Δr_{mas}
5	0.09 ± 0.01	24.6 ± 2.8	0.56 ± 0.07
8.4	0.16 ± 0.01	14.6 ± 1.7	0.34 ± 0.04
10.6	0.20 ± 0.02	11.6 ± 1.3	0.27 ± 0.03
22.2	0.42 ± 0.04	5.5 ± 0.6	0.13 ± 0.02

Notes: the offsets of the core from the true jet origin are given for a jet with $\theta = 5^{\circ}$.

in the jet from the equipartition regime. The relativistic particle energy density $\varepsilon_p \propto T_b^{4.5}$, and the the energy density in the magnetic field $\varepsilon_B = B^2/8\pi \propto T_b^{-4}$. This gives $\varepsilon_p/\varepsilon_B \approx (T_{b\,max}/T_{b\,eq})^{8.5} \approx 2 \times 10^8$, for the ultracompact jet, and therefore the jet is not in the equipartition regime, and must lose its energy through X-ray emission due to inverse Compton scattering. Unwin *et al.* (1994) argue that, farther down the jet, in the superluminal features C4 and C5, the physical conditions may also deviate from the equipartition significantly. According to Unwin *et al.* (1994), $\varepsilon_p/\varepsilon_B \sim 10^2 - 10^4$ in C4 and C5, which is a natural consequence of evolution and radiation losses in a plasma with original $\varepsilon_p/\varepsilon_B \sim 10^8$.

To calculate the magnetic field in the core, and the core distance from the true jet origin, we use formulae 6.25 and 6.22. Table 6.1 summarizes the derived positions and magnetic field of the VLBI core of 3C 345 at different frequencies. According to the derived positions, the location of the core observed at 22 GHz should be about 5 pc away from the jet origin. This may support the particle cascade models (see Section 6.1.2), and the model of a self–similar inner jet (Marscher 1995). Each of these models require the observable radio jet to be formed at a substantial distance from the central energy source. The angular offsets are all smaller than the VLBI beam size at given frequency; therefore, the central engine is likely to be blended with the VLBI core even if the opacity is low enough for the emission from the innermost regions of the jet to be observed. Under such circumstances, evidence for emission from the inner jet can only be found in the spectral index or turnover frequency maps.

In Figure 6.4, the derived magnetic field is compared with the values obtained from the synchrotron emission calculations for C2, C3, and C4 (Zensus, Cohen, and Unwin 1995), as well as with the model predictions for the central engine in 3C 345. The magnetic field in the superluminal features is derived from fitting their spectra by optically thin, spherical blobs emitting synchrotron radiation. The theoretical values of the magnetic field in the close vicinity of the central engine are adopted from the model of Field and Rogers (1993) for a thin magnetically driven accretion disk, and from the model of a supermassive black hole surrounded by a strong magnetic field (Kardashev 1995). The accretion disk model predicts $B \approx 10^4$, and ≈ 160 G at $r \approx R_g$, and $\approx 24 R_g$, correspondingly ($R_g = 2GM_{bh}/c^2$ is the Schwarzschild radius of the central black hole). For the mass of the black hole in the center of 3C 345,

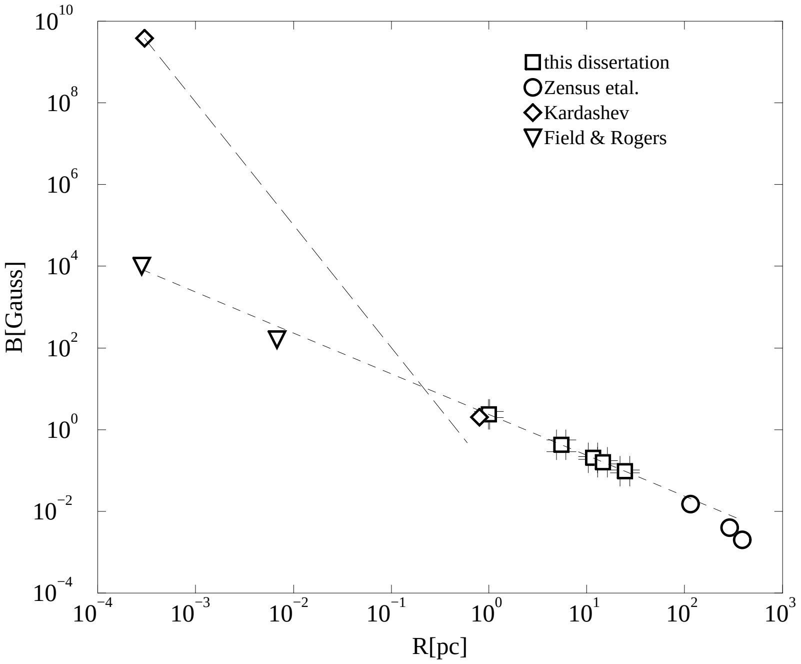

Figure 6.4: Magnetic field distribution in 3C 345. Squares show the magnetic field in the compact jet derived in this dissertation from the frequency dependent shift of the core. Circles are the SSC-based estimates of the magnetic field in the outer jet components C2, C3 and C4 (Zensus *et al.* 1995). Triangulars show the characteristic magnetic field estimates from a model of magnetized accretion disk (Field and Rogers, 1993). Diamonds are the theoretical estimates from Kardashev's (1995) model for the dipole magnetic field around a supermassive rotating black hole.

we follow the estimates made by Kardashev (1995), and assume $M_{bh} \sim 6 \times 10^9 \mathrm{M}_\odot$. Kardashev suggests that a strong dipole magnetic field may exist in the vicinity of supermassive black hole. The maximum field strength can be then estimated from the equilibrium relations $M_{bh} \sim M_d \sim M_B$, where M_{bh}, M_d, M_B are masses of black hole, its disk, and its magnetic field respectively. Then $B_{max} = c^4 G^{-1.5} M_{bh}^{-1}$. This gives for 3C 345: $B_{max} \approx 3.3 \times 10^9$ G. The magnetic field of a rotating black hole is dipole ($B \propto r^{-3}$), so that $B \leq 1.7$ G at 0.8 pc. The latter prediction is consistent with our estimates $B_1 \approx 2.4$ G.

6.3.2 Core shift in other sources

In the absence of multifrequency positional astrometry measurements, applying the measured (or even just estimated) shift of the core may provide a first order approach to alignment of VLBI maps, and better understanding of the results obtained from

Table 6.2: Predicted core position shift between 5 and 22 GHz

Name	Type	$\Delta r_{5,22}$ [mas]	L_{syn} [erg/s]
3C 273	LPQ	0.78	2.4×10^{43}
3C 216	HPQ	0.70	3.1×10^{43}
3C 120	LPQ	0.61	8.4×10^{41}
4C 39.25	LPQ	0.57	2.2×10^{44}
NRAO 512	BL	0.55	1.3×10^{41}
1807+698	BL	0.26	3.3×10^{41}
BL Lac	BL	0.11	2.3×10^{41}

spectral index maps. If the derived dependence (4.3) and the Königl's model hold for other sources, then the magnitude of core shift can be estimated from the total synchrotron power L_{syn} given by equation (6.51). If the jet has its observed opening angle ϕ_{ob}, and moves with Lorentz factor γ at an angle θ to the line of sight, then the expected offset of the observed core position between frequencies $\nu_{1,2}$[GHz] will amount to:

$$\Delta r[\mathrm{mas}] \approx \frac{2.2 \times 10^{-31}}{\gamma^2 \phi_0} \cdot \frac{\nu_1 - \nu_2}{\nu_1 \nu_2} \cdot \frac{Z\, h}{Z - Z^{0.5}} \cdot \left[\frac{L_{syn} \sin\theta}{\beta(1 - \beta\cos\theta)\ln(\frac{r_{max}}{r_{min}})} \right]^{2/3}, \quad (6.53)$$

for a source at redshift $z = Z - 1$ (with $q_0 = 0.5$ and $H_0 = 100h$ km s^{-1} Mpc^{-1}).

Table 6.2 gives predicted core position shifts between 5 and 22 GHz for a few prominent radio sources.

6.3.3 Applicability of the shock based schemes

The shock-in-jet model was used to explain the total flux variations in AGN, primarily in blazars (e.g. Marscher *et al.* 1991, Hughes, Aller & Aller 1989b). Most of the applications have so far been made for single antenna observations in which it is not possible to separate the compact structure emission from the extended emission, or to isolate the emission from individual knots in the VLBI scale jet. Total flux variations have been ascribed to the core and its immediate vicinity. Variability of the extended emission has been neglected, since it is known to have generally smaller amplitudes and longer time scales than those found in the compact structures. However, distinguishing between different features of the jet itself may be more crucial for studying the applicability of different jet models. Therefore, in this section, we will first attempt to find a region of the jet chiefly responsible for the source variability exhibited in the single antenna observations.

The contributions of different parts of the source to its total emission at 22 GHz are shown in Figure 6.5. The flux densities shown are normalized to the maximum

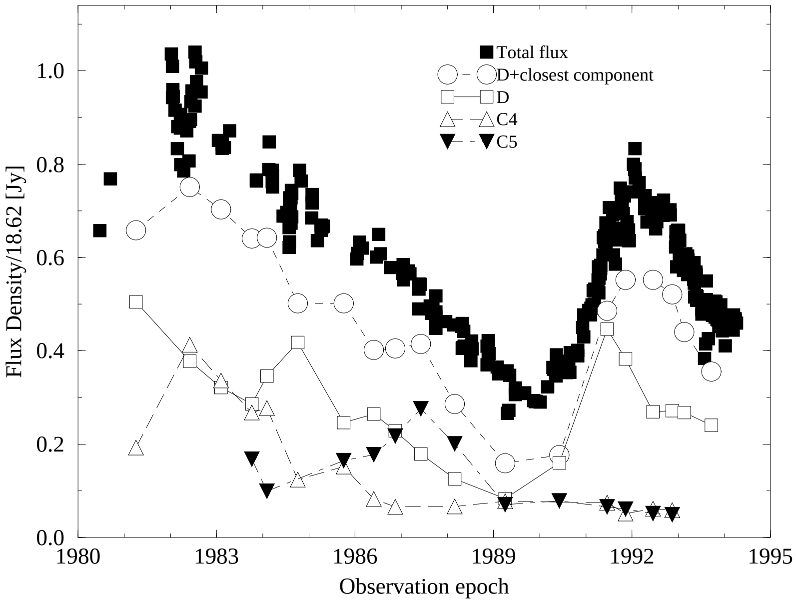

Figure 6.5: Contributions of VLBI features to the total emission of 3C345 at 22 GHz. Black squares denote the single dish measured flux density. White circles are the cumulative flux density of the core and a closest component or an emitting complex located within ≈ 1 mas distance from the core (the *conical jet*). Total flux density is normalized to the maximum total flux of 18.62 Jy observed in 1982. Flux densities of the constituent components are fractions of the total flux density.

total flux of 18.62 Jy. Calibration errors of the VLBI data were processed using the procedure described in Chapter 4.

In Figure 6.5, neither of individual features (D, C4, or C5) can represent the total emission evolution. Therefore, the emission dominating the total emission changes is most likely to come from several VLBI features of the source. We consider an extended emitting complex which includes the core and the closest superluminal component (white circles in Figure 6.5).

The biggest separation of the closest component was observed at the epoch of 1988.16 for C5 being 1.2 mas away from the core. This separation determines a region extended over $\approx 4.5h^{-1}/\sin\theta_{C4}$ pc from the core (θ_{C4} is angle between the component's instantaneous velocity and the line of sight). We hereafter refer to this region as the *conical jet*, following the terms from Blandford and Königl (1979).

As seen in Figure 6.5, the flux evolution of the conical jet is correlated with the total flux evolution. Correlation between the core and the total flux, although still visible, is not as good as that between the total flux and the conical jet. The core flux shows a sharp rise from late 1983 to late 1984 when a new component (C5) was emerging. This effect, however, does not seem to be represented in the total flux data. Before and after that rise, the core flux declines exhibiting approximately the same slope as that in the conical jet and total flux. And so does the flux of C4 up until

1987, when it seems to become nearly constant. The slowing down of flux decrease can be an indication that shock mechanisms are no longer dominating the component emission, implying a significant influence of plasma interactions and reacceleration occurring at these spatial scales in the jet. In this case, a pure shock scenario would fail. Therefore we will use the criterion of non–decreasing component flux to estimate the ranges of applicability for the shock models

The separation between D and C4 was 1.2–1.3 mas in 1987, marking up roughly the same extension as that of the conical jet. The similar change in the flux evolution of C5 occurs at ≈1.7 mas corresponding to the linear distance of $\approx 6.4h^{-1}/\sin\theta_{C5}$ pc.

Figure 6.5 shows that total flux is dominated by the compact emitting complex in the source. Thereby, this emission is being effectively accounted for in the above-mentioned relativistic–shock models. The extension of this complex can be of the order of $5h^{-1}/\sin\theta$ pc. However, intrinsic changes of the emitting features constituting the parsec–scale structure remain masked, and are not present in the total flux evolution. In particular, there is no indication of the appearance of C5, despite its share of the total flux had reached the level of 30% in 1987. Also, the latest stages of component flux evolution exhibit properties incompatible with pure adiabatic expansion, and there should be some additional mechanism employed, in order to explain an extended lifetime of the moving components. Some of the possibilities for such a mechanism include: a) continuous injection of a relativistic plasma into the jet; b) variations of the Doppler boosting factor due to changing kinematic conditions in the jet; c) plasma interactions and non–shock reacceleration of a plasma in the jet.

6.3.4 Variable injection of a relativistic plasma

It is possible, in principle, to explain different types of spectral evolution in the superluminal knots by a variable injection of relativistic plasma. However, the continuous injection is model dependent, and the VLBI data we have are not sufficient to allow us to draw a conclusion with regards to whether or not a certain scheme with variable injection rate would be satisfactory for describing the observed peaked spectral evolution in C4 and C5.

It seems reasonable that the plasma injection would influence mostly the emission in two extremes of the shock evolution: at the stage when the formation of a new shock is underway, but before it becomes supersonic; and at the epoch when the shock falls off, matching the parameters of a quiescent jet again. In the intermediate epochs, the Lorentz factor γ_s of a shock propagating down the jet is exceeding that of the bulk motion (γ_j), and injection is likely to be significant only for the reverse shock propagating backwards with respect to the forward shock (cf. Marscher 1990). In this case, it might be possible to detect a spectral difference between the forward and reverse shocks, using simultaneous multifrequency VLBI observations and a subsequent continuous restoration of the synchrotron spectrum. The injection can be more prominent for the weak shocks which may remain in the state of adiabatic expansion through their entire evolution (Hughes *et al.* 1989). On the later stages of adiabatic expansion, injection of a plasma with the energy spectrum qE^{-s} would cause slowing down a decrease of the shock flux F_ν, since $F_\nu \propto t^{-s}$ (Kardashev 1962) as opposed to $\propto t^{-2s}$ for an expansion without injection (Shklovsky 1960). The plasma injection does not seem to be enough to account for the observed flux evolution of C4, particularly because the observed flux remained virtually constant over the last 5 years, and the observed energy spectral index of C4 was very steep ($s_{C4} \approx 4.3$ already in 1987).

6.3.5 Variable Doppler factor

In this section, we investigate the possibility that the observed spectral evolution can be explained by changes of Doppler factor alone. As it was shown in Chapter 3, the jet components of 3C345 show a steady increase of the apparent velocities. The observed increase of apparent velocities and Doppler factor $\delta(t)$ both can be ascribed either to instantaneous acceleration of a straight jet ($\theta = const$):

$$\frac{d\delta(t)}{dt} = \frac{\beta - 2\beta^2\cos\theta + \cos\theta}{(1-\beta^2)^{1/2}(1-\beta\cos\theta)^2} \cdot \frac{d\beta}{dt}, \tag{6.54}$$

or to changes of Doppler factor due to curvature of the jet ($\gamma_j = const$):

$$\frac{d\delta(t)}{dt} = \frac{(1-\beta^2)^{1/2}\beta\sin\theta}{(1-\beta\cos\theta)^2} \cdot \frac{d\theta}{dt}. \tag{6.55}$$

From jet kinetic energy considerations, the latter choice appears to be more realistic. In reality, of course, it is possible that both θ and γ_j are varying simultaneously. For sake of simplicity, we will not consider the latter possibility in this paper.

There are three arguments in favor of changes in Doppler factor in the jet patterns: a) extended time evolution of the component emission; b) apparent acceleration of the components; c) observed spectral evolution of the component emission incompatible with monotonic decline of the turnover frequency predicted by the simple relativistic shock models (Marscher & Gear 1985). The model used by Marscher (1990) describes spectral evolution in terms of the turnover frequency ν_m, the peak flux density S_m, and the flux density S_ν at $\nu \gg \nu_m$. The model implicitly assumes that the Lorentz factor is constant in time and that the light travel time effects do not change the proportionalities significantly. In what follows, we discuss the influence of variations in Doppler factor on the predictions of the relativistic shock model.

6.3.6 Relation between spectral and kinematic evolution

From the condition of monotonic decline of the turnover frequency, we can assume that its evolution obeys the conditions

$$\frac{d\nu'_m(t')}{dt'} < 0, \quad \text{and} \quad \frac{d\nu'_m(t')}{dt} = C_0(t) < 0 \tag{6.56}$$

where the primed quantities are in the rest frame of the jet, $t = t'\delta(t)^{-1}$ is time in the frame of the observer and $C_0(t)$ is an arbitrary function.
Taking into account relativistic Doppler shift of frequency, and reformulating (6.56) for the extremum condition $d\nu_m/dt = 0$, we can write

$$\frac{d\nu_m}{dt} = C_0\delta + \frac{1}{\delta}\frac{d\delta}{dt}\nu_m = 0 \tag{6.57}$$

Note that the explicit time dependences of ν_m, C_0 and δ are omitted in (6.57).
In order to explain existence of a maximum in the turnover frequency evolution, the Doppler factor must change with time so that

$$\frac{d\delta}{dt} = -C_0\frac{\delta^2}{\nu_m} \tag{6.58}$$

Obviously, $d\delta/dt > 0$ in all cases, and therefore only an increasing Doppler factor can reproduce the observed spectral evolution of the jet components. This increase may be due to the intrinsic acceleration, or changing geometry of the jet, or both (see equations (6.54), (6.55)). To compare the prediction of (6.58) with the observations, we express the Doppler factor δ as a function of distance r traveled by a shock, and then we transform it to a function of time in the observer's frame.

Denoting the power indices in (6.30)–(6.32) with ϵ and formulating the condition of extremum for ν_m, we then obtain

$$\frac{d\nu_m}{dt} = \epsilon r^{\epsilon-1}\frac{dr}{dt} = 0 \tag{6.59}$$

Since the trivial cases $t = 0$ and $\beta(t) = 0$ are easily ruled out by the observations, the only physically meaningful solution of (6.59) is

$$\epsilon = 0 \tag{6.60}$$

Equation (6.60) determines the loci of b as a function of m and s in each of the three stages of shock development such that they cover the particular combinations of b, m, and s which are necessary for the turnover frequency to assume a maximum value. These combinations are shown in Figure 6.6 for different values of m ranging from $m = 1.0$ to $m = 2.0$.

6.3.7 Evolution of C4 and C5

Since b is defined by the relation $\delta \propto r^b$, it represents, in Figure 6.6, the magnitude of apparent shock acceleration required at a certain stage of shock development to achieve a peak in the evolution of the turnover frequency. It is clearly seen from Figure 6.6 that the peak is not likely to occur at the adiabatic–loss stage, as the acceleration required in this case is too high, and it is increasing with steepening of the electron energy spectral index s. At the stage of synchrotron losses, a peak can be possible for

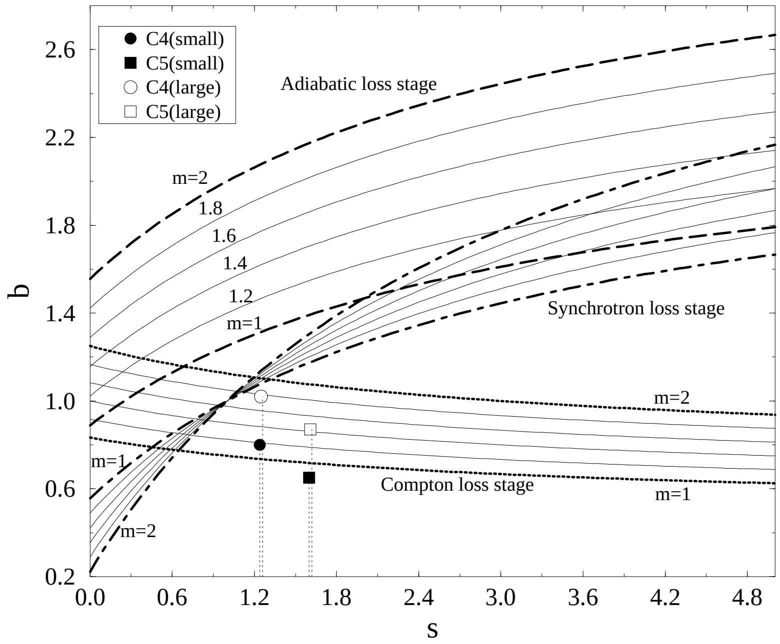

Figure 6.6: Conditions of existence of a maximum in the time evolution of the turnover frequency ν_m expressed through the energy spectral index s, and constants m and b describing the evolution of magnetic field and Doppler boosting along the jet. Circles and squares represent the upper limits of b calculated for C4 and C5 respectively, at the epochs of maximum turnover frequency in each of the components (see text, also).

a shock with flat energy spectral index, although b is increasing most rapidly in this case, quickly achieving the values comparable to those of the adiabatic–loss stage. The most likely candidate for the location of a peak in the turnover frequency evolution is the Compton–loss stage, since the acceleration required in this case becomes smaller with steepening the energy spectral index and aging of a shock.

In order to calculate the values of b, we analyze the kinematic evolution of C4 and C5. For these components, we take the apparent velocities β_{app} derived in Chapter 3, equation (3.6). Considering the extreme cases of an entirely intrinsic ($\theta = const$) and entirely apparent ($\beta = const$) acceleration in the jet, we calculate the changes of Doppler factor, δ, and the rest frame distance, r, of the jet components from the core. The red shift dependence, time dilation, and relativistic aberration were taken into account in assumption of the standard cosmological model (see equations (3.9)–(3.11) in Chapter 3). Assuming that the VLBI core corresponds to the "injection point" in

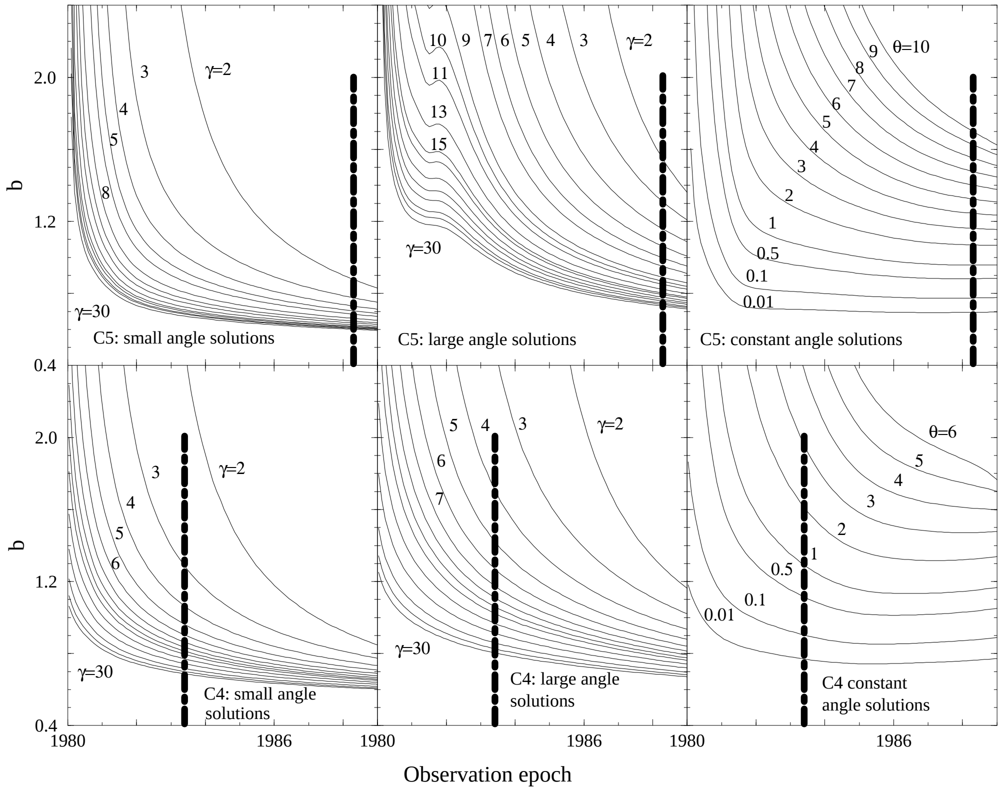

Figure 6.7: Factor b represented in different kinematic solution for C4 and C5. The upper panels show the small–angle, large–angle, and constant–angle solutions for C5; the same solutions for C4 are shown in the lower panels correspondingly. Thick dot–dashed lines indicate the epoch of maximum turnover frequency for each component (1983.4 for C4, and 1988.3 for C5).

the shock–in–jet model, we can then determine b

$$b = \frac{\log \delta}{\log r}\,. \tag{6.61}$$

Because there are two solutions for θ in case when $\beta = const$, there are three possible cases that must be considered: the *small–angle* solution, the *large–angle* solution, and the *constant–angle* solution corresponding to $\theta = const$ (see Sections 3.3.1, 3.3.1 of Chapter 3 for a description of these solutions). The solutions are shown in Figure 6.7 for C5 (upper row) and C4 (lower row). Different curves represent the solutions obtained for different γ and θ, from the polynomial fits for C4 and C5 listed in Table 3.1. These curves trace the changes of b under various kinematic conditions. It is seen in Figure 6.7 that b decreases with increasing γ and decreasing θ. Thick dot–dashed lines drawn in the panels are marking the epochs of maximum turnover frequency for each component (1983.4 and 1988.3 for C4 and C5, correspondingly).

The constant angle solutions fail, in general, to describe the jet's kinematics in the beginning of the components evolution. For both C4 and C5, all solutions for

Table 6.3: Kinematical and spectral parameters of C4 and C5.

Component	α^a	s^b	$\gamma_{min}{}^c$	$b_{small}{}^d$	$b_{large}{}^e$
C4	-0.12	1.24	9.81	0.80	1.02
C5	-0.30	1.60	5.50	0.65	0.87

Notes: a – 11–22 GHz spectral index at the epoch of maximum turnover frequency; b – energy spectral index at the epoch of maximum turnover frequency; c – minimum kinematically allowed Lorentz factor; d – b–factor derived for the small angle solution; e – b–factor derived for the large angle solution.

$\theta \geq 1$ are unstable and predict drastic changes of b from positive to negative values (not shown in Figure 6.7) close to the epoch of a component's origin. It is unlikely that the instantaneous velocity of a jet would undergo such changes, and therefore we will not use the $\theta = const$ solutions, to determine b.

The large–angle solutions and the small angle solutions in the case $\gamma = const$ are much more consistent over a wide interval of Lorentz factors. The difference between these two types of solutions is that the large angle solutions require a faster moving jet, and therefore they yield higher values of b. This will require a stronger initial acceleration of the jet, which poses certain theoretical difficulties for finding an appropriate mechanism capable of reproducing such speeds and accelerations. Another argument against the large–angle solutions is that they require uncomfortably large variations of the viewing angle (see Section 3.3.2 of Chapter 3). Because of these considerations, we favor the small–angle kinematic solutions as the most plausible for the interpretation of the jet's spectral properties. Because the exact values of the component Lorentz factors are unknown, we can only determine the upper limits of b–factors. To find the upper limits of b, we use the lowest kinematically allowed Lorentz factor $\gamma_{min} = (1+\beta_{app})^{1/2}$, and calculate the corresponding value of maximum kinematically allowed of b–factor at the epoch of maximum turnover frequency of a given component The upper limits of the b–factors are given in Table 6.3, alongside with other spectral and kinematic parameters of C4 and C5.

The energy spectral index is calculated from the spectral index measured between 11 and 22 GHz at the epoch of the maximum turnover frequency. The corresponding b–factors are plotted in Figure 6.6. The open circle and open square correspond to the large–angle solution, the filled ones mark the small–angle solution.

In the jets with turbulent acceleration of $e^{\pm}$ plasma, the maximum bulk Lorentz factor is not likely to exceed $\gamma = 20$ (Abramovicz 1992; Henri & Pelletier 1992). If we suppose that $\gamma_{C4} = 20$, then its b–factor from the small–angle solution will satisfy precisely the conditions for a transverse magnetic field ($m = 1$) in a shock. From the b–factors in Figure 6.6, we can suggest that the maximum turnover frequency may occur rather at the Compton loss stage, and that at least one component (C4) can be satisfactorily explained in the frame of the shock–in–jet model with variable

Table 6.4: Kinematic and flux parameters of C4 and C5.

	C4	C5
Origin epoch, t_0	1979.5	1980.0
Maximum ν_m epoch, t_m	1983.4	1988.3
Distance traveled at t_m [pc]†	$3.0h^{-1}$	$5.3h^{-1}$
Flat flux distance [pc]†	$4.6h^{-1}$	$6.4h^{-1}$
γ_{min}	10	6
S_{max} at 22 GHz [Jy]	5.9	3.0
S_{max} at 11 GHz [Jy]	8.1	6.0
S_{max} at 5 GHz [Jy]	3.6	4.3

Notes: † – without accounting for the projections $\propto (\sin\theta_j)^{-1}$

C2: t_0=1968.0 C3: t_0=1976.0 C3a: $t_0 = 1977.5$ C6: $t_0 = 1987.5$ C7: $t_0 = 1988.0$

Doppler boosting. For C5, we can argue that the observed peaked evolution of the turnover frequency in this component is unlikely to be caused by variation of Doppler factor. This conclusion is consistent with C5 being generally the weaker component noticeably differing in its manifestations from C4.

Table 6.4 gives an overview of the kinematic and physical characteristics of C4 and C5. The components appear to be different in every aspect, except for their epochs of origin which are separated by only about six months. For a comparison: time separation between the appearances of C4 and C3 is 3.5 years, and it is about 8 years for C2 and C3. This can suggest that C4 and C5 can be the product of the same outburst.

One of the possible physical explanations can be that, in case of C4 and C5, we are dealing with the forward and the reverse shocks in the jet. The strength of C4, and its possible relation with C3a can be an additional argument for possible formation of a reverse shock. In this case, C5 also should be a weaker shock, or a product of both shock and plasma interactions. The maximum occurred in the evolution of its turnover frequency could rather be due to physical factors such as interaction with non–relativistic plasma and reacceleration. Another explanation can be sought in the model of an elliptically distorted helical jet (Hardee *et al.* 1995), in which case C4 and C5 would be representing the same or two consecutive distortions propagating down the jet.

6.3.8 Transition zone in the jet

Several independent observational facts seem to indicate that a transition may occur in the jet, at about 1.2-1.5 mas separation from the core.

1) ZCU95 have found that the component trajectories and velocities change rapidly in the vicinity of the core. Farther along the jet, these changes become less evident, and the component trajectories are nearly straight.

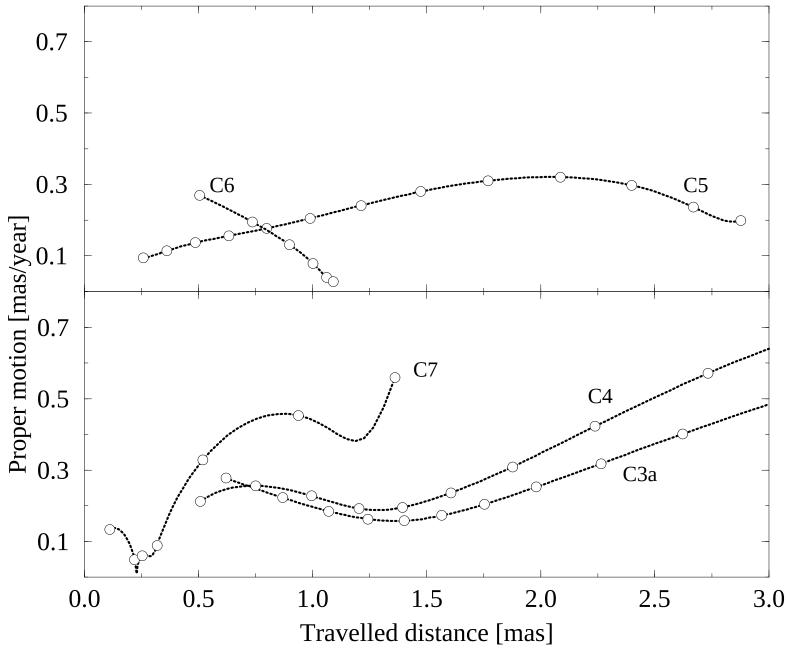

Figure 6.8: Proper motion of the strong and weak jet features in the vicinity of the core. The minimum is seen for the strong features, at distances $\approx 1.5 - 2$ mas from the core. The components C1, C2, and C3 are outside the plotting ranges.

2) The proper motions of the strong jet features show a deceleration, with the minimum speed achieved at about 1.5 mas traveled distance. After that, the components accelerate up to the speed of 0.9 mas/year.

3) The 11 and 22 GHz flux density of the strong components show a fast rise succeeded by a sharp fall, within 0.1-1.5 mas distance from the core (Figure 6.9). Such behavior is characteristic for shocks, and most of the shock models applied to the jet features of 3C 345 were describing the emission at this stage. Father away from the core, the flux densities decline slowly. Such a slow decline may not be readily reproduced by the shock scenario.

4) Correlation between the total and parsec–scale emission of 3C 345 seems to indicate that relativistic shocks are most prominent within about 1.2 mas distance from the jet core.

5) From the polarization measurements, the magnetic field orientation seems to change from being predominantly transverse at small scales (Leppänen 1995) to longitudinal at larger scales. This implies the presence of strong shocks close to the core, and their subsequent yielding to other mechanisms producing the observed polarization (i.e. plasma interactions, and formation of a shear layer).

A scheme in Figure 6.10 summarizes the observational evidences for a transition zone in the jet. One of the possible implications of Figure 6.10 is that unshocked emission may be responsible for an increasingly larger fraction of the jet emission

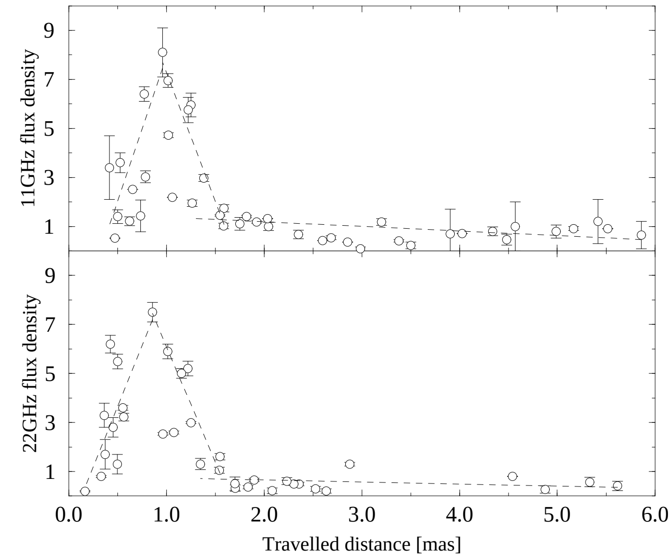

Figure 6.9: Flux changes in the strong jet features at 11 and 22 GHz. The flux densities of C2, C3, C3a, C4, and C7 are plotted as a function of traveled distance. The sharp rise and fall are normally explained by shocks; the long low–flux tail may be produced by interactions between different plasma components of the jet.

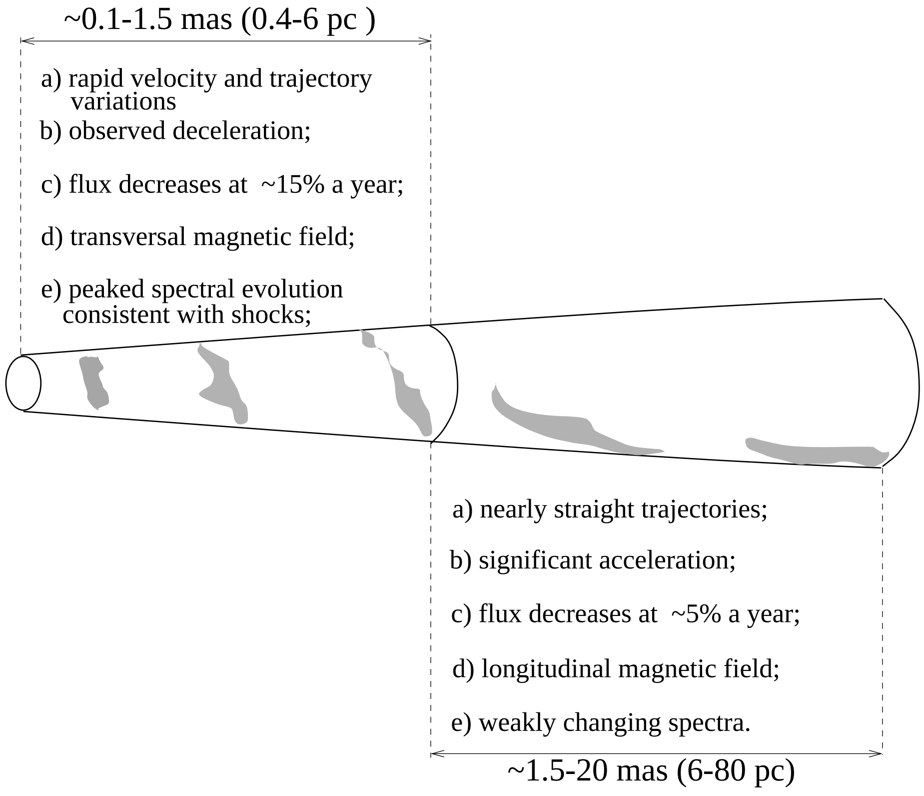

Figure 6.10: Possible transition in the jet of 3C345.

beyond ≈ 2 mas distance from the core. The shocked and unshocked components of the jet emission may coexist along the entire parsec–scale jet, each dominating in different regions of it. Gabuzda *et al.*(1995) have reported a detection of a new-born VLBI feature (possibly, still in a pre-shock stage) with longitudinal magnetic field, in the BL Lacertae object 1219+285. This observation supports the simultaneous existence of shear-dominated and shock-dominated emission in the jet. The shear-dominated emission can be due to an interaction between the relativistic plasma and ambient medium (in a transition zone from the broad line to the narrow line region, Gabuzda *et al.*1995). Alternatively, the relativistic plasma in the jet might interact with a thermal outflow produced in the outer regions of accretion disk (Sol *et al.* 1989). Similar model with two interacting flows has been proposed for kiloparsec–scale jets (Laing 1993).

6.4 Summary

The main results of this chapter can be summarized as follows:

1) The physical conditions in the ultra–compact jet of 3C 345 have been studied. The magnetic field strength in the VLBI core is calculated, using the measured offset of the core position at different frequencies. The calculated values agree well with the measurements made for superluminal features in the jet of 3C 345, as well as with the prediction by a model for a magnetized accretion disk. An estimate of the brightness temperatures was made from the derived magnetic field. The obtained value is higher than the equipartition value, indicating that the total energy of the ultra–compact jet is dominated by the relativistic particle energy. The latter condition should result in significant X-ray flux due to inverse Compton scattering.

2) The applicability of the shock–based schemes is studied. The results from comparison of the total and VLBI flux evolutions at 22 GHz suggest that shock based models describe preferentially the emission from a very compact region around the source core. For 3C345, the extension of this region is found to be $\approx 5\,h^{-1}/\sin\,\theta$pc.

3) The shock–in–jet model is applied to the observed evolution of the turnover frequency of C4 and C5 (the turnover frequency changes are discussed in Chapter 5). A modification of the model is introduced, so as to account for variable Doppler factor. The model predictions are compared with the spectral and kinematic changes observed in C4 and C5. We have shown that the peaked evolution of the turnover frequency in C4 complies with the relativistic shock at the stage of Compton losses. For C5, only the large–angle kinematic solution can satisfy the model requirements. As we argued in Chapter 3, the large–angle solutions are incapable, in general, of explaining the observed component trajectories and apparent velocities. Therefore, we can suggest that factors other than variable Doppler boosting must have influenced the observed spectral changes of C5.

4) On the basis of comparison between the flux, kinematic, and spectral properties of C3a, C4, and C5, we suggest that these three jet components can be related in

their origins. It is possible that C3a, and C4 represent two forward shocks, and C5 is a reverse shock originated from the same outburst in the core.

5) Several independent observations are gathered, in support of existence of a transition zone between the shock–dominated and plasma interaction–dominated regions in the jet of 3C 345.

Chapter 7

Conclusion

The data accumulated from the VLBI monitoring of 3C345 provide an extended account of morphology, kinematics, and radio emission from the parsec–scale regions in the source. The long–term evolution can be studied in the individual jet features, as well as in the jet as a whole, using the VLBI data. On the basis of such study, a general picture of the physical processes in the parsec–scale jets can be attained. In this chapter, we summarize briefly the main conclusions made about the jet kinematical and emission properties, in an attempt to link them together and present an overview of the compact regions in 3C345. In the last section of the chapter, we discuss some prospective directions for studying the compact jets.

7.1 Parsec–scale structures in 3C345

7.1.1 Morphology and kinematics

The observed morphology of 3C345 is typical for a core dominated source: a bright and compact core containing most of the compact–scale emission, and a compact jet consisting of several enhanced emission regions (jet components). With improving dynamic range of VLBI maps, the underlying emission also becomes observable, revealing the factual continuity of the jet. The bright jet components move outwards with apparent velocities of up to $\beta_{app} \approx 20h^{-1}$. There are also marginal indications for existence of subluminal motions, in the close vicinity of the source core.

The compact VLBI jet of 3C345 extends over about 20 mas which corresponds roughly to an $80\,h^{-1}$ pc linear extension. The length of the jet is marked by the distinct turn from $\phi_{VLBI} \approx -70°$ to $\phi_{VLBI} \approx -40°$ observed between 15 and 20 mas separations from the core. The latter is consistent with the position angle of the large–scale scale jet of 3C345, $\phi_{VLA} \approx -40°$. A sharp increase of the jet width observed at distances larger than 15 mas also suggests that the transition from the compact jet to larger–scale jet occurs in this region.

Closer to the core, there are two other twists observed in the jet at the separations of $\approx$1 and $\approx$5 mas. The twists appear to retain their positions in the jet, over long periods of time. Such stability of the twists suggests that they are likely to reflect the three–dimensional curvature of the jet. The unchanged positions of the twists are also consistent with the similarities of the component apparent trajectories, at separations larger than 1 mas. The observed apparent trajectories are most likely to be produced by the actual helical trajectories of the components. However, the observed changes of apparent velocities in the jet components cannot be explained by variations of the viewing angle alone. Physical acceleration is required, in order to explain the observed apparent acceleration of the components. That is, the component Lorentz factors should change along the jet.

Kinematically, the components can be separated into three groups corresponding to the outer jet (4–20 mas; C1, C2, C3), intermediate jet (1–4 mas; C3, C3a, C4, C5), and inner jet ($\leq$1 mas; C6, C7). The outer jet is characterized by nearly straight trajectories and fast apparent speed. In the intermediate jet, the components tend to have significant accelerations. The inner jet presents rapid and sharp variations of component velocities.

Younger jet components tend to have higher proper motion than that of the older components, at the same separation from the core. This fact may reflect a global kinematical evolution of the jet. The global changes are most likely to be caused by the jet precession resulting in more favorable viewing angles for more recent jet features.

On the outer and intermediate jet scales, the relationships between the constituent jet components are likely not to be limited only to the kinematical similarities. The estimated epochs of origin of the intermediate jet components may indicate that they were produced by a single event (or a short series of related events) occuring in the core of the source. C3a and C4 may also represent the result of a split of a powerful jet feature. The compound morphology of C3 and C4 observed at the later epochs supports the possibility of a jet component breaking up into several distinct features.

7.1.2 Emission

By comparing the flux and kinematical evolutions of the jet components we are able to distinguish between strong and weak features. The strong components (C2, C3, C3a, C4, and C7) are generally faster and brighter. The apparent velocities of these components follow roughly the same evolution path, with increasing separation from the core (the characteristic feature of the observed velocity evolutions is the presence of a local minimum at approximately 1.5–2 mas distance from the core). In addition to the similarity of kinematical parameters, the flux curves of C3, C4, and C7 show approximately the same rates of flux decrease ($\approx$15% a year, at the early stages of the decrease; and $\approx$5% a year, at the latest stages of the decrease). The rise and decline of the core flux are similar to the flux changes in the strong components.

Contrary to the similarities found in the strong components, the weak components (C5, C6) neither resemble each other, nor the stronger features. C5 shows a slow flux rise; later, the flux drops abruptly by almost 60–80% within one year. The trajectory of C5 is significantly curved, and the component velocity does not have a local minimum observed in the strong jet components. C6 has extremely low 22 GHz flux; the component velocity decreases down to subluminal values; the component becomes hardly detectable at 1 mas separation from the core. Such peculiarities of C5 and C6 make it possible to suggest that the observed differences are caused not only by pure geometrical factors, but also by different physical conditions existing in these components.

The evolution of the rest–frame luminosity of C4 is different from the luminosity changes observed in the core and C3, C4, and C5. The difference is not likely to be explained by the kinematical factors, unless the Lorentz factor of C4 changes, and the component accelerates in the rest frame of the jet.

Synchrotron spectra of the core and the jet component show profound changes and correlations. The integrated 4–25 GHz flux rises, with increasing turnover frequency of the spectrum. The correlation between the integrated flux and the turnover frequency is weak for the core and very clear for the component. The turnover frequency of the core remains high at all epochs. This can be explained by a continuous injection of relativistic plasma, or by permanent blending of the core and the nearest shocked feature of the jet. Another argument in favor of blending is that the turnover frequency of the core rises every time when a new superluminal feature appears.

The turnover frequencies of C4 and C5 show peaked evolutions. Both C4 and C5 emerge having low turnover frequency in their spectra. The turnover frequency rises for a few years, and declines afterwards. This can be a consequence of physical and/or kinematical changes occuring in the components. Analyses show that, for C4, the maximum of the turnover frequency can be explained by a relativistic shock with changing Doppler factor. Similar analyses carried out for C5 result in the conclusion that kinematical factors alone are not likely to explain the observed changes of the component turnover frequency.

Overall, C4 and C5, although having very close epochs of origin, are proven to have radically different kinematical properties, flux evolutions, and spectral changes. On the basis of the observed differences between C4 and C5, we may suggest that C5 represents a reverse shock, while C4 is a forward shock — with both C4 and C5 produced by the same outburst. Another alternative would be to consider the elliptical distortions in the jet as a possible source for appearances of double features.

7.1.3 Shocks and plasma interaction

The bright features observed in parsec–scale jets are usually explained by shocks existing in ultrarelativistic flows. Shocks are able to explain observed variations in the total flux and polarization of many compact radio sources.

When the total flux evolution of 3C345 is compared to the flux changes of individual parsec–scale features, it becomes evident that variations of the total flux are determined at large by the emission coming from the very close vicinity of the core ($\leq$1.2 mas). Thus, we can expect that the shock based scenarios can successfully explain this region of the source. The observed properties of the ultracompact jet in 3C 345 strongly suggest that this region is dominated by the emission coming from an ultrarelativistic, shocked plasma.

At larger separations from the core, there are several observational facts that are difficult to be explained by the shock models. The component life times exceed expected life times of relativistic shocks. The kinematical and luminosity evolution of the jet components suggest the presence of significant intrinsic acceleration. This fact is not predicted by the shock models. The slowing down of the component flux decrease suggests an additional mechanism supporting the emission of jet components. The observed changes of the polarization can also indicate a possible evolution of physical conditions along the jet.

The abovementioned facts all lead to a suggestion of plasma interactions as a possible source for prolonging the component life times, and reacceleration of the bright features. In the two–fluid scenario, a relativistic plasma can interact with a thermal outflow, and produce the emission enhancement necessary for an explanation of the latest stages of the component evolution. So far, we have only indirect indications to the possible existence of two fluids in 3C345: in the turnover frequency distribution map, the longitudinal feature with high turnover frequency may be identified with the relativistic channel. Other patterns seen in the turnover frequency map can also reflect the velocity and/or density gradient in a jet perturbed by Kelvin–Helmholtz instability. There are also evidence for perturbed, helical–type motions of the superluminal jet features in the immediate vicinity of the core.

Several pieces of observational evidence are pointing at the possibility of a transition from the shock–dominated to plasma interaction–dominated emission regime existing in the jet of 3C 345. It is possible that both shocks and plasma interactions play equally important roles in the parsec–scale emission: shocks being responsible for the initial, most violent stages of component evolution, and plasma interactions providing the observed manifestations of the jet emission on more extended spatial and time scales.

7.2 Prospective work

The observed physical properties of the parsec–scale jet in 3C 345 (and of parsec–scale jets in general) seem to be overly complex to be explained in the frameworks of simple models, and within a single emission mechanism. The evidence for the existence of several distinct zones in the jet arise from a variety of observational results. Both advanced observations and more detailed numerical simulations are needed for reconstructing the physics of the jets. High–resolution polarization observations (possibly with VSOP) should give a better picture of magnetic field evolution in the immediate vicinity of the jet core. Measuring the spectral properties and the velocity distribution across the jet would answer the question of the existence, and properties of, an underlying jet, and of a shear layer. Numerical models concentrated on reproducing an extended lifetime of the jet components should be able to evaluate the importance of plasma interaction on parsec–scales. A few immediate suggestions for continuations of the study include the following topics:

1) Continuation of the monitoring with multifrequency VLBA observations. Using the multifrequency data for spectral index mapping and continuous analysis of the synchrotron spectra of the jet. We expect to be able to verify the presence of a relativistic channel, shock fronts, and plasma instability patterns inside the jet.

2) Modeling of the global kinematical evolution in the jet. Using the constraints provided by the global changes of the jet apparent velocities, we will attempt to produce a model that would be able to explain both the individual component trajectories, and the changes of the trajectories of successive components.

3) Modeling of the forward and reverse shock evolution. This model would be used for comparing with the data on C4 and C5. Other possible candidates for the model to be applied to is C6 and C7.

4) Two–fluid scheme: emission from parsec–scale regions. A model describing the emissive properties of a two–fluid jet is necessary for undertaking quantitative analysis of the extended evolution of the jet components.

5) Incorporating polarization imaging into the scope of the study. Polarization information would provide necessary constraints on the properties of magnetic field in the jet, as well as on the Lorentz factors of the components.